Abrupt Topological Transitions in the Hysteresis Curves of Ferromagnetic Metalattices

J. E. Han and Vincent H. Crespi

Department of Physics and Materials Research Institute, The Pennsylvania State University, 104 Davey Lab, University Park, Pennsylvania 16802-6300

(Received 5 February 2002; published 22 October 2002)

When a metal is confined to the interstices of an inert colloidal crystal, the intrinsic order parameter(s) of electronic and magnetic phenomena within the metal interact with the structural order parameter of the surrounding (and confining) colloidal crystal. If the magnetic stiffness length is comparable to the colloidal lattice constant, the interplay of competing interactions stabilizes multiple topologically distinct magnetic phases separated by sharp transitions in the hysteresis curves. The colloidal confinement also induces substantial coercivity in metals that are perfectly soft in the bulk.

DOI: 10.1103/PhysRevLett.89.197203 PACS numbers: 75.75.+a, 75.60.-d

In the well-known cases of zero-, one-, and two-dimensional quantum confinement, (i.e., dots, wires, and thin films), the low-temperature dynamics in free dimension(s) is largely decoupled from the discretized degrees of freedom in the confining directions. Here we describe an alternative regime of confinement wherein the confined and extended degrees of freedom cannot be separated: an ordered three-dimensional superstructure (or metalattice [1]) that confines an infiltrant, yet also permits extended states therein. If the electronic states of an infiltrant metal possess, in the bulk, an order parameter with a characteristic length scale comparable to the lattice constant of the confining superstructure, then the structural order parameter of the metalattice can interact richly with the intrinsic order parameter of the infiltrant metal. Several such examples can be envisioned, including normal metals [1] (scattering lengths, etc.), superconductors (penetration depth and coherence length), and ferromagnets (e.g., the exchange stiffness length). In this Letter, we focus on one archetypal example: a ferromagnet infiltrated into the interstitial spaces of a nonmagnetic face-centered cubic colloidal crystal. The well-ordered magnetic confinement within this ferromagnetic metalattice stabilizes a sequence of unusual intermediate magnet phases, each with distinct topological character; these are separated by sharp magnetically induced phase transitions wherein the microscopic magnetization texture abruptly changes local curl, divergence, and/or direction. In essence, the familiar bulk demagnetization factor of a macroscopic sample is translated into a nanometer-scale intrinsic material property with fascinating consequences for the range of accessible microscopic states. This confinement can also induce a nonzero coercivity with values ranging up to a few kilogauss. Infiltrated metallic metalattices are beginning to be synthesized by filling the interstices of close-packed colloidal crystals [2,3].

Since experimentally accessible monodisperse colloidal spheres have diameters ranging from tens to thousands of nanometers, we concentrate on continuum-level magnetic properties rather than the detailed atomic-scale structure. To isolate the essential physics, we treat a minimal set of magnetic interactions, the exchange energy and the magnetostatic energy, within a $2 \times 2 \times 2$ supercell of an fcc colloidal lattice. This supercell loosens the constraints due to periodic boundary conditions and permits domain formation within the supercell. Later we discuss possible extensions to larger systems and other structures, once the basic physics is in hand.

In the continuum limit, the nearest-neighbor exchange interaction contributes to the energy density a term

$$A[(\nabla m_1)^2 + (\nabla m_2)^2 + (\nabla m_3)^2], \tag{1}$$

where A (> 0) is the exchange stiffness and $\mathbf{m} \equiv \mathbf{M}/M_s = (m_1, m_2, m_3)$ is the magnetization normalized with respect to the saturation magnetization M_s. In our calculations, $|\mathbf{m}| \approx 1$ to within a few percent.

The magnetostatic energy provides a crucial geometrical contribution within a ferromagnetic metalattice, since the dipole-dipole interaction prefers a magnetization that aligns parallel to the interface. The magnetostatic energy density (in cgs units) is

$$E_{\text{mag}} = -\tfrac{1}{2}\mathbf{M}(\mathbf{r}) \cdot \mathbf{H}'(\mathbf{r}) = -\tfrac{1}{2}M_s^2 \mathbf{m}(\mathbf{r}) \cdot \mathbf{h}'(\mathbf{r}). \tag{2}$$

The dipole field $\mathbf{H}' \equiv M_s \mathbf{h}'$ is

$$\mathbf{H}'(\mathbf{r}) = \int_V d^3\mathbf{r}' \frac{3\hat{\mathbf{n}}[\hat{\mathbf{n}} \cdot \mathbf{M}(\mathbf{r}')] - \mathbf{M}(\mathbf{r}')}{|\mathbf{r}' - \mathbf{r}|^3}, \tag{3}$$

where $\hat{\mathbf{n}}$ is the unit vector along $\mathbf{r}' - \mathbf{r}$ and V extends over the entire sample [4]. Finally, the energy density due to the external field $\mathbf{H}_{\text{ext}}$ is $-\mathbf{H}_{\text{ext}} \cdot \mathbf{M}(\mathbf{r})$. Combining these contributions and rescaling to a dimensionless length $\mathbf{x} = \mathbf{r}/D$ with the diameter of colloidal sphere D, the total energy density becomes

$$E = M_s^2[\tfrac{1}{2}d^{-2}|\nabla \mathbf{m}|^2 - \tfrac{1}{2}\mathbf{m} \cdot \mathbf{h}' - \mathbf{h}_{\text{ext}} \cdot \mathbf{m}]. \tag{4}$$

The dimensionless diameter $d = D/\sqrt{A/M_s^2}$, while the dimensionless external field $\mathbf{h}_{\text{ext}} = \mathbf{H}_{\text{ext}}/M_s$. The resulting magnetization has a scaling form

$$\mathbf{M}(\mathbf{r}) = M_s \mathbf{f}(\mathbf{r}/D, \mathbf{H}_{\text{ext}}/M_s; d). \tag{5}$$

Within this approximation, d governs the magnetic behavior; an increase in the exchange stiffness A is equivalent to a decrease in the colloidal lattice constant. For specificity, we use the exchange stiffness and saturation magnetization of bulk Ni (i.e., $A = 0.82 \times 10^{-11}$ J/m, $M_s = 0.53 \times 10^{-6}$ A/m [5,6]); the results can then be scaled to represent other materials.

To constrain the magnitude of the magnetization to the vicinity of M_s, we add to the square bracket of Eq. (4) a potential $-\frac{\alpha}{2}|\mathbf{m}|^2 + \frac{\beta}{4}|\mathbf{m}|^4$ with positive α and β. For α and β of order $\sim$10, the magnetization $|\mathbf{m}|$ differs from 1 by less than 10%, and the results described below are insensitive to the specific values chosen.

We ignore crystalline anisotropy and magnetostriction. Although including them requires only a modest computational effort, the simpler model adopted here most clearly reveals the new effects of confinement which arise from the competing length scales of the exchange stiffness and metalattice structure. In addition, the composition of magnetic alloys can be tuned to obtain conditions of low crystalline anisotropy and magnetostriction [7].

We start in the well-defined high-field state and gradually decrease the external field, sweeping the field until a converged hysteresis loop results. At each point on the hysteresis curve, the configuration from the previous magnetic field value (with a small amount of noise added) provides the initial state for successive conjugate gradient [8] energy minimizations. We use a $32 \times 32 \times 32$ mesh point grid, also of fcc symmetry. Adequate spatial resolution [9] was confirmed by tests on denser grids in a system with a single primitive cell.

The primitive cell of the fcc lattice contains one octahedral interstitial site and two tetrahedral sites, each filled with magnetic material and bounded by nonmagnetic spheres (see Fig. 1). The sizes of these sites and the connections between them are crucial to determining the magnetic behavior. The magnetostatic energy is minimal when the local magnetization curves around the void surfaces and thereby avoids terminating in a free surface. However, excessive curvature increases the exchange stiffness energy. The thin necks between the infiltrant sites impose the strongest constraint: the magnetization tends to stream along the necks. For example, Fig. 1 shows the most stable neck configuration when a moderately strong external field points along (001). The magnetization on faces (111), $(1\bar{1}1)$, $(\bar{1}11)$, and $(\bar{1}\bar{1}1)$ points outward while that on faces $(11\bar{1})$, $(1\bar{1}\bar{1})$, $(\bar{1}1\bar{1})$, and $(\bar{1}\bar{1}\bar{1})$ points inward. The tetrahedral sites each have two faces with inward magnetization and two with outward magnetization. The configuration for the external field along (001) is the most symmetric and has the lowest energy. Therefore, metalattice confinement imposes a (001) easy axis on an isotropic bulk magnetic infiltrant.

We first discuss the simplest case: an external field along the easy axis, (001). In the limit of small colloidal spheres [10] ($D \lesssim 40$ nm), the magnetization in each infiltrant site aligns perfectly with the external field (as seen in Stoner-Wohlfarth theory for hard magnets [11]). Because of the cubic symmetry, the effective dipoles arising from the demagnetization fields on the surfaces of each spherical void feel no net magnetostatic interaction from the surrounding dipoles [12]. Therefore, the coercivity is zero in the limit $D \to 0$. The reversal is then a one-step transition, as shown in the top plot in Fig. 2(a). A simple dimensional argument shows that (for a defect-free isotropic system) the coercivity increases as $H_c \sim M_s d^2 \sim M_s^3 D^2/A$ at small D [see Fig. 2(a)]. This confinement-induced coercivity can exceed 1 kG even for soft magnets such as permalloys.

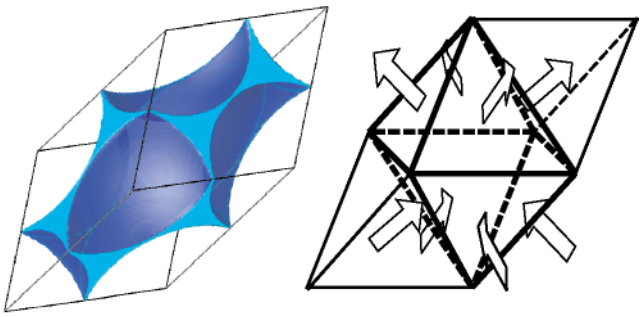

FIG. 1 (color online). Left: The tetrahedral and octahedral interstitial spaces of an fcc colloidal lattice (with spheres centered at the vertices) are filled with ferromagnetic material. Intersections of necks with the cell edges are in light gray. Right: The primitive infiltrant cell within a single fcc cell, with colloidal spheres on each vertex. The necks between filled sites penetrate each face. Arrows show magnetization directions in the necks for a moderately strong external field pointing upward, along (001).

As the lattice constant increases, the magnetic moments in the necks soften and more complex magnetic patterns begin to form. The first such phase is a stacking of ferromagnetic planes that are antiferromagnetically coupled to each other. For $D = 90$ nm at A_2 in the middle plot in Fig. 2(a), the magnetic state in each layer aligns with the (001) axis as shown in Fig. 3(a). The magnetization curls around the colloidal sphere surfaces; this circulating magnetization mediates the antiferromagnetic coupling between layers.

The coercivity maximum of Fig. 2(a) (which lies close to the transition between soft and hard behavior) occurs at $\ell_{\mathrm{mag}} \sim 4\sqrt{A}/M_s$, comparable to the characteristic magnetic length scale of the system, as expected. At larger lattice constants, the magnetization gradually begins to conform more closely to the void surfaces to minimize the magnetostatic contribution. When $D \gtrsim \ell_{\mathrm{mag}}$ [i.e., the bottom plot in Fig. 2(b) with $D = 200$ nm], the hysteresis loop develops a precursor at B_2 before the magnetization jump. This precursor signals the onset of substantial magnetic curling [13] within the octahedral site, as shown in Fig. 3(b). The magnetization spirals around the (001) axis; the local magnetization has a positive (001) component in addition to a nonzero circulation. The magnetic ring appears only inside the octahedral

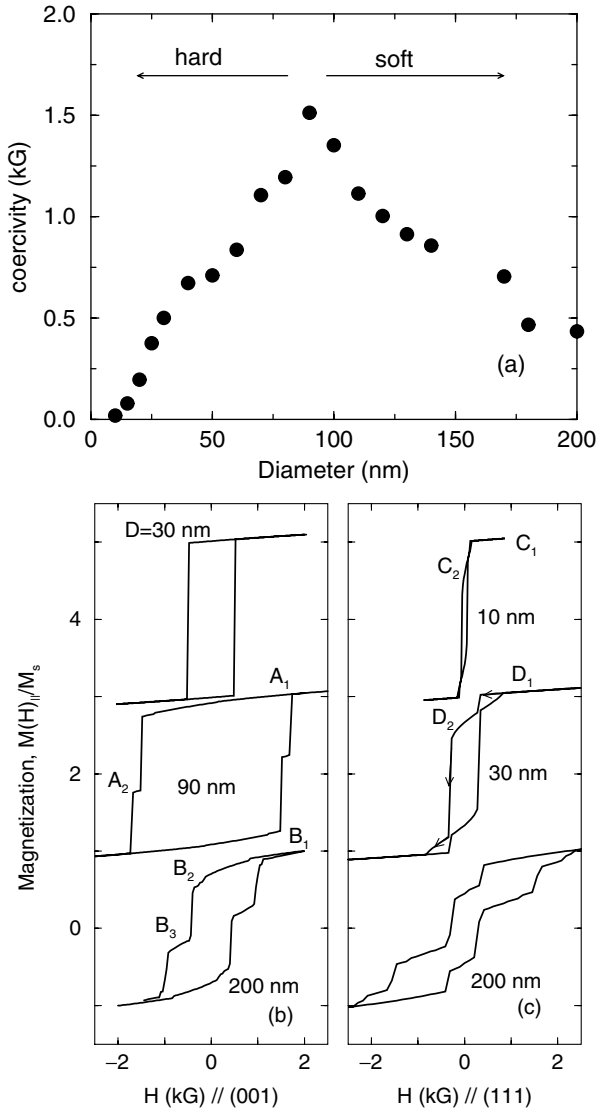

FIG. 2. Top: The coercivity as a function of colloidal sphere diameter D with the external field in the easy direction, (001). At $D \ll \ell_{\mathrm{mag}}$, the system behaves as a hard magnet. For $D > \ell_{\mathrm{mag}}$, the system better accommodates gradual changes in magnetization and behaves like a soft magnet. The coercivity peaks near $D \sim \ell_{\mathrm{mag}}$. Bottom left: Hysteresis loops for an external field along (001). At $D = 30$ nm, the magnetization aligns parallel to the field. At $D = 200$ nm ($D > \ell_{\mathrm{mag}}$), the reversal traverses several stages of local energy minima. Bottom right: The magnetization along a noneasy axis (111). The reversal is triggered at a smaller external field, is softer, and passes through more complex local minima.

sites because the tetrahedral ones are too small to accommodate a strong spatial variation in magnetization. The octahedral sites also have higher (fourfold) symmetry along the (001) axis than the (twofold) tetrahedral sites. The handedness of this rotation is arbitrary and decided by the numerical noise.

The system makes another transition to B_3 as the external field continues its reversal. At the B_2-B_3 transition, the magnetic spirals uncoil and the average magnetization in each octahedral site settles into one of the easy-axis configurations. These local dipoles are primarily governed by the local anisotropy of the underlying colloidal lattice and the magnetically floppy necks provide only weak intersite interactions. Because of the degeneracy of the easy axes (for an external field aligned

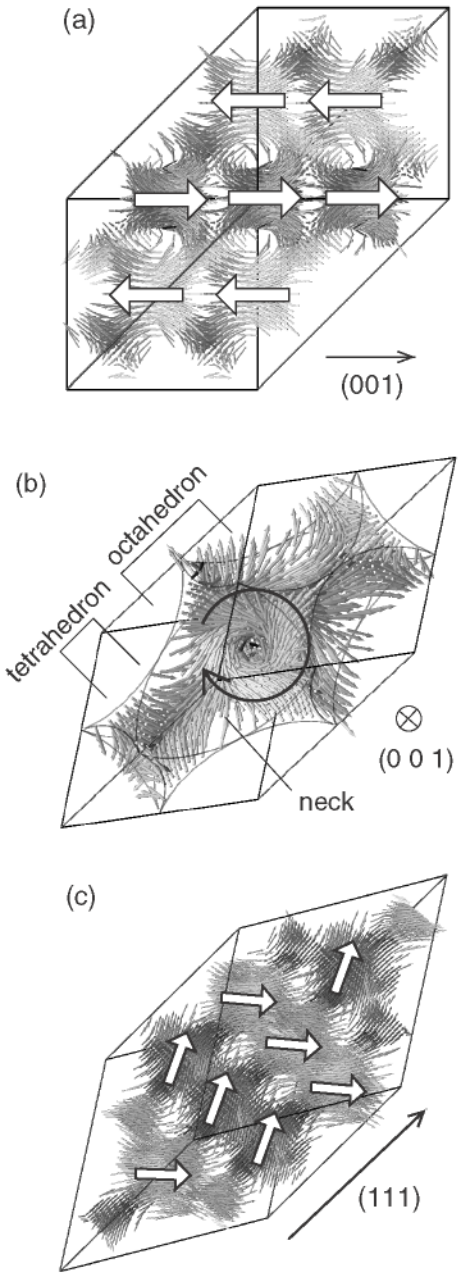

FIG. 3. (a) Layered ferromagnetism at $D = 90$ nm with **H** along (001) (A_2 of Fig. 2). Layered ferromagnetic domains form normal to (001). (b) The magnetic ring along (001) inside an octahedral site, showing only a single cell of the supercell (B_2 of Fig. 2). This magnetization pattern minimizes the magnetostatic energy. (c) Layered ferromagnetism at $D = 30$ nm with **H** along (111) (D_2 of Fig. 2). The layer planes are normal to (111) and the magnetization within the domains is along one of the easy-axis directions.

with a symmetry direction), the global magnetic configuration in this phase has a high degeneracy and the small random noise in the simulation chooses a particular configuration. It is interesting to consider whether this highly degenerate system with trifold intersite interactions would be prone to any glasslike magnetic behavior.

External fields along noneasy axes can yield a yet richer set of transitions due to the competing influences of the external field and the easy axis. The coercivity maximum still appears at the roughly same value of D. For an external field along (111), the hysteresis curve even in the hard-magnet regime [i.e., the top two curves in Fig. 2(c)] has a quite different structure from that for an easy-axis field. At high fields (C_1) the magnetization is forced along the (111) axis. At lower fields the system jumps between successive easy-axis directions along the path to complete reversal, forming patterns of increasing complexity as the lattice constant increases. At small d, the magnetization in the intermediate state (C_2 in the top curve) aligns along an easy direction before undergoing an abrupt transition to the reversed state. When the magnetic length scale falls below the supercell size, ferromagnetic substructures begin to appear. At $D = 30$ nm, the intermediate state again splits into layers (D_2 in the middle figure), but this time perpendicular to the (111) direction [see Fig. 3(c)]. The magnetization within the domains can take any of the (100), (010), or (001) directions, since the external field and layer normal align with (111).

At a large lattice constant ($D = 200$ nm), the system is magnetically more compliant and therefore generates an ever-increasing number of intermediate states. The local magnetizations of the octahedral sites are still in the easy-axis directions, but the intersite correlations become more complex as the exchange-coupling constraints from the connecting necks weaken and the long-range dipolar interactions become more important. The hysteresis curves still show abrupt jumps in magnetization between distinct phases [see the bottom curve in Fig. 3(c)]. As the metalattice size increases, sample inhomogeneities will eventually wash out the sharp structures in the globally averaged magnetization, although a rich local dynamics should survive. In this regime, it may be possible to ignore the neck-mediated exchange coupling between adjacent octahedral sites and instead treat the system in terms of effective dipole-dipole interactions between octahedral sites to elucidate the larger-scale dynamics. Since the magnetization patterns within the simulation supercell already optimize the demagnetization field on a small scale, the tendency to domain formation on larger scales should be weaker than for an equivalent bulk magnet. Nevertheless, larger-scale domain structures should appear in the limit of increasing D.

The competition between magnetic stiffness, demagnetization fields, and geometrical constraints within ordered nanoscale matter opens several avenues for further interesting physics. For example, the transition involving a spiraling magnetization pattern may be tunable by external currents along the axes of the spiral. Spin waves within such structures may exhibit optical branches. At finite temperatures, entropic factors will contribute to relative phase stability along the hysteresis curves. The phases with patterns of local moments or local spirals on octahedral sites could be treated with effective interactions to study larger-scale and statistical properties. Disorder in colloidal size and packing will lend further avenues for investigation. Finally, metalattice superconductors provide a natural extension of this length-scale competition to a new physical regime, with prospects for inducing effective or intermediate type I/II behavior, among other physics.

We gratefully acknowledge support from the David and Lucile Packard Foundation, the Penn State Materials Research Science and Engineering Center under NSF Grant No. DMR-0080019, and the Penn State Materials Simulation Center.

[1] J. E. Han and V. H. Crespi, Phys. Rev. Lett. **86**, 696 (2001).
[2] G. L. Egan, J.-S. Yu, C. H. Kim, S. J. Lee, R. E. Schaak, and T. E. Mallouk, Adv. Mater. **12**, 1040 (2000).
[3] D. Kang, J. E. MacLennan, N. A. Clark, A. A. Zakhidov, and R. H. Baughman, Phys. Rev. Lett. **86**, 4052 (2001).
[4] To eliminate additional anisotropy, we have chosen a spherical sample with a diameter much larger than the colloidal lattice constant.
[5] J. Weissmüller *et al.* J. Res. Natl. Inst. Stand. Technol. **104**, 261 (1999).
[6] Parameters for hard-magnet clusters are almost the same as in bulk down to 100 nm; S. A. Nepijko and R. Wiesendanger, Europhys. Lett. **31**, 567 (1995).
[7] Charles Kittel, Rev. Mod. Phys. **21**, 541 (1949).
[8] M. C. Payne, M. P. Teter, D. C. Allen, T. A. Arias, and J. D. Joannopoulos, Rev. Mod. Phys. **64**, 1045 (1992).
[9] M. J. Donahue and R. D. McMichael, Physica (Amsterdam) **233B**, 272 (1997). An excellent guide to magnetic modeling can be found at www.ctcms.nist.gov/~rdm/mumag.org.html.
[10] As the colloidal dimension approaches the atomic scale, crystalline effects, such as polycrystallinity or alloy domains, could dominate over magnetostatic effects.
[11] E. C. Stoner and E. P. Wohlfarth, Nature (London) **160**, 650 (1947).
[12] J. D. Jackson, *Classical Electrodynamics* (Wiley, New York, 1975), 2nd ed., pp. 152–155. This ignores the bulk demagnetization field due to the macroscopic sample surfaces.
[13] A. Aharoni and S. Shtrikman, Phys. Rev. **109**, 1522 (1958).